NEU-2021-0451-ver9-Maugeri_1P
Type: Research Article

Journal of Neurotrauma
39:1–14 (2022)

DOI: 10.1089/neu.2021.0451

Journal of Neurotrauma

Open camera or QR reader and scan code to access this article and other resources online.

ORIGINAL ARTICLE

Lesion Extension and Neuronal Loss after Spinal Cord Injury Using X-Ray Phase-Contrast Tomography in Mice

Laura Maugeri,[1–3] Aleksandar Jankovski,[4,5] Emil Malucelli,[6] Fabio Mangini,[3] Jean-Michel Vandeweerd,[7] Jacques Gilloteaux,[8,9] Kathleen De Swert,[8] Francesco Brun,[10] Ginevra Begani Provinciali,[11,12] Mauro DiNuzzo,[3,13] Alberto Mittone,[14,15] Alberto Bravin,[15,16] Giuseppe Gigli,[2] Federico Giove,[1,13] Alessia Cedola,[11] Charles Nicaise,[8*] and Michela Fratini[3,11*,**]

Abstract

Following a spinal cord injury (SCI) the degree of function (motor, autonomous, or sensory) correlates with the severity of nervous tissue disruption. An imaging technique able to capture non-invasively and simultaneously the complex mechanisms of neuronal loss, vascular damage, and peri-lesional tissue reorganization is currently lacking in experimental SCI studies.

Synchrotron X-ray phase-contrast tomography (SXPCT) has emerged as a non-destructive three-dimensional (3D) neuroimaging technique with high contrast and spatial resolution. In this framework, we developed a multi-modal approach combining SXPCT, histology and correlative methods to study neurovascular architecture in normal and spinal level C4-contused mouse spinal cords (C57BL/6J mice, age 2–3 months). The evolution of SCI lesion was imaged at the cell resolution level during the acute (30 min) and subacute (7 day) phases. Spared motor neurons (MNs) were segmented and quantified in different volumes localized at and away from the epicenter. SXPCT was able to capture neuronal loss and blood–brain barrier breakdown following SCI. Three-dimensional quantification based on SXPCT acquisitions showed no additional MN loss between 30 min and 7 days post-SCI. In addition, the analysis of hemorrhagic (at 30 min) and lesion (at 7 days) volumes revealed a high similarity in size, suggesting no extension of tissue degeneration between early and later time-points. Moreover, glial scar borders were unevenly distributed, with rostral edges being the most extended. In conclusion, SXPCT capability to image at high resolution cellular changes in 3D enables the understanding of the relationship between hemorrhagic events and nervous structure damage in SCI.

AU1 ▶ [1]CNR-Institute of Nanotechnology, Rome Unit, Rome, Italy.
[2]CNR-Institute of Nanotechnology, Lecce Unit, Lecce, Italy.
[3]IRCCS Fondazione Santa Lucia, Rome, Italy.
[4]Université catholique de Louvain (UCLouvain), Institute of NeuroScience (IoNS), NEUR Division, Brussels, Belgium.
[5]Department of Neurosurgery, Université catholique de Louvain (UCLouvain), CHU UCL Namur, Yvoir, Belgium.
[6]Department of Pharmacy and Biotechnology, University of Bologna, Bologna, Italy.
[7]URVI-NARILIS, [8]URPhyM-NARILIS, Université de Namur, Namur, Belgium.
[9]Department of Anatomical Sciences, St George's University School of Medicine, Newcastle upon Tyne, United Kingdom.
[10]Department of Engineering and Architecture, University of Trieste, Trieste, Italy.
AU2 ▶ [11]CNR-Institute of Nanotechnology c/o Physics Department, Sapienza University, Rome, Italy.
[12]Laboratoire d'Optique appliquée, ENSTA Paris Tech, Palaiseau, France.
[13]Museo Storico della Fisica e Centro Studi e Ricerche Enrico Fermi, Rome, Italy.
[14]CELLS-ALBA Synchrotron Light Source, Barcelona, Spain.
[15]European Synchrotron Radiation Facility, Grenoble, France.
[16]Department of Physics, University of Milano-Bicocca, Milan, Italy.
*The last two authors contributed equally.

AU12 ▶ **Address correspondence to: *Michela Fratini, Istituto di Nanotecnologia, Consiglio Nazionale delle Ricerche, Piazzale Aldo Moro 2, 00185, Rome, Italy E-mail:* michela.fratini@gmail.com

Keywords: quantification; spinal cord injury, synchrotron X-ray phase-contrast tomography

Introduction

After spinal cord injury (SCI), primary and secondary mechanisms are cumulatively involved in the irremediable nervous tissue damage.[1] The primary SCI insult causes immediate vascular rupture, disruption of passing fibers, and neuronal loss.[2]

As early as 5 min post-SCI, Nissl bodies disappear from neuronal perikarya followed by cell death, a process that culminates between 4 and 8 h post-injury at the epicenter.[3–6] During the subacute phase, spared neurons, adjacent to the initial epicenter, enter in apoptosis.[4,5,7] Meanwhile, the recruitment of immune cells and activation of resident glial cells produce a plethora of inflammatory mediators and free radicals, which further compromise the immediate peri-lesional tissue homeostasis.[1,2] Consequently, the secondary lesion extension is thought to be responsible for the worsening of the functional outcomes commonly observed in patients.[1,4–7] It is admitted that the extent of the primary injury predicts the neurological outcomes following SCI.[8,9] Consequently, the number of spared neurons represents a key prognostic factor.

The evaluation of neuron integrity within a complex cell network with powerful imaging tools is a very demanding task. Therefore, innovative biomarkers or three-dimensional (3D) imaging modalities must be continuously developed. Even though post-mortem magnetic resonance imaging (MRI) is a useful technique for the 3D analysis of central nervous system (CNS) tissue,[10–13] it lacks the spatial resolution needed to access the neuron scale. Conventional X-ray tomography can partially overcome this resolution limit, but it fails to produce high-contrast images from soft tissues. Although histology reaches (sub-) cellular resolution, it is a destructive procedure subject to preparation bias and lacking faithful 3D rendering abilities.

MRI, X-ray tomography, and histology limitations can be overcome by synchrotron X-ray phase-contrast tomography (SXPCT). SXPCT is a non-destructive 3D imaging technique, able to visualize low-absorbing tissue samples such as biological tissue, thanks to the high sensitivity to phase-shifting due to the differential intrinsic electronic densities in the biological tissues.[14,15] Previous *ex vivo* studies validated SXPCT as a tool to visualize simultaneously the architecture of vascular and neuronal networks in the mouse spinal cord, down to a 100-nm resolution, without contrast agent or tissue sectioning.[16–18] Moreover, with full 3D scans, it is possible to align cords to root entry zones and perform raw 3D volume measurements, without calling for time-consuming stereological methods.[19] Hence, SXPCT has been applied on *ex vivo* mouse and rat spinal cords following SCI. Most of the experimental SCI studies focused on the evolution of the cystic cavity, the remodeling of blood vessels post-SCI, and the effect of various angiogenic modulating strategies.[19–26] Although the cystic cavity or the spinal vascular network was easily reconstructed using tomography, none of the aforementioned studies was able to visualize the neuronal loss or the cells involved in the building of the peri-lesional scar.

Thanks to potentiality, the high resolution of SXPCT, ◀AU3 the present work characterized, for the first time, the changes of spinal cell distribution in a mouse model of cervical SCI as well as spinal tissue reaction and remodeling post-SCI.

We observed that the peri-lesional cells accumulated in an inhomogeneous distribution, showing the highest cellular infiltration and thickness rostral to the epicenter, compared with all other directions. Even though the glial scar border is only mature several weeks' post-injury, this finding will help to better define glial scar ablating strategies. In particular, we imaged the morphological evolution of the lesion with a single-cell spatial resolution affording the discrimination of neuronal subpopulations and glial cells based on differential phase-shifts. Such a finding would have been difficult to capture using classical two-dimensional (2D) serial sectioning methods.

Methods

Experimental design and animals

Fifteen male C57BL/6J mice, age 2–3 months, were included in the study. The experimental protocol (reported below in the Methods section, and in Supplementary Appendix S1) ◀SA1 was conducted in compliance with the European Communities Council Directives for Animal Experiment (2010/63/EU, 86/609/EEC, and 87–848/EEC) and was approved by the Animal Ethics Committee (ethics project UN 17-284). ◀AU4

Mice were divided into three groups, each including five animals: (1) uninjured, (2) C4-injured followed by euthanasia 30 min post-SCI, and (3) C4-injured followed by euthanasia 7 days post-SCI. We did not include a 12–24 h timing with the most prominent blood extravasation. We deliberately chose: 30 min post-SCI, a subacute SCI timing characterized by a significant amount of red blood cells (RBCs) accumulating into the spinal parenchyma; and 7 days post-SCI, an acute-to-chronic SCI timing, when the microhemorrhage process is being resolved, but not fully.

SCI protocol

Mice were anesthetized with a cocktail of ketamine (100 mg/kg) and xylazine (5 mg/kg) delivered intraperitoneally. The skin along the midline, between the spinous

processes of spinal cord level C2 and T1, was incised to expose the mid-cervical region. The epaxial muscle layers were dissected and retracted, and muscles overlying C4–C6 were removed. The uninjured sham-surgery group underwent a laminectomy at C4, but did not receive contusion injury. Injured mice were subjected to a unilateral, right-sided, C4 spinal contusion using the computer-controlled Infinite Horizon Impactor (Precision Systems and Instrumentation, Lexington, KY, USA) with a force set at 5×10^{-4} Newton as previously described.[27,28] Animals were monitored on a daily basis, and measures were taken to avoid dehydration and to minimize any potential pain (subcutaneous administration of buprenorphine: 0.1 mg/kg twice a day during first 48 h). Using the same anesthesia cocktail, mice were euthanized by exsanguination and transcardial perfusion with NaCl 0.9% followed by phosphate-buffered 4% paraformaldehyde. The spinal cords were post-mortem harvested, further fixed in paraformaldehyde for 48 h, and kept in phosphate-buffered saline (PBS) at 4°C until imaging session. Spinal cords were *ex vivo* imaged with SXPCT in free space propagation mode without the use of contrast agents.[15]

Synchrotron X-ray phase contrast tomography setup

The experiments were carried out at the TOMCAT beamline of the Swiss Light Source (SLS) located in Villigen, Switzerland, and at the ID17 beamline of the European Synchrotron Radiation Facility (ESRF) located in Grenoble, France.

TOMCAT beamline. The incident monochromatic X-ray energy was of 17 keV. A PCO.edge 5.5 camera coupled with optics resulting in a pixel size of $0.65 \times 0.65\ \mu m^2$ (field of view [FOV] = $1.7 \times 1.4\ mm^2$) and $1.64 \times 1.64\ \mu m^2$ (FOV = $4.2 \times 3.5\ mm^2$), respectively, was set at a distance of 5 cm from the sample. The tomography was acquired with 2751 projections (pixel size of $1.64 \times 1.64\ \mu m^2$) and 3351 projections (pixel size of $0.65 \times 0.65\ \mu m^2$), covering a total angle range of 360 degrees.

ID17 beamline. The incident monochromatic X-ray energy was of 30 keV and the distance between the sample and the detection system was set at 2 m. The detection system[29] consists of a PCO.5.5 sCMOS detector coupled with optics systems to obtain a final pixel size of $3.07 \times 3.07\ \mu m^2$ (FOV = $7.6 \times 6.4\ mm^2$). The tomography was acquired with 2000 projections covering a total angle range of 360 degrees. The entire volume of the spinal cord was measured. The tomographic projections were reconstructed using Syrmep Tomo Project (STP).[30] After the beamtime, the samples were sectioned and further processed for histological analysis (see Supplementary Appendix S1).

Synchrotron X-ray phase contrast tomography data analysis

Neuron counting. Spinal cells, including neurons, were unambiguously visualized by SXPCT due to the different electronic densities of the soma and of the nucleus (or even of the nucleolus in the case of motor neurons [MNs]). Based on the different gray levels, the more intense nuclear region can be told apart from the soma. The discrimination of spinal cells was performed on the basis of their soma size[31] as suggested by the cell-size profiling obtained by histology methods (Supplementary Fig. S1). MN counting was carried out on tomographic images pre-processed by an adaptive threshold method. MNs in rodents are typically 20–35 μm in diameter, with MN subsets less demarcated in size. The size exclusion represents the most-used criterion to discriminate MN from non-MN populations and is widely used for counting (for a review see the article by Ferrucci and colleagues[32]).

The counting was performed by choosing a voxel size corresponding to the real volume of the neurons, as previously estimated by profiling the size distribution of the most common spinal cells in histology, based on the expression of specific markers (NeuN/neurons, SMI32/MNs, glial fibrillary acidic protein [GFAP]/astrocytes, p25α/oligodendrocytes, Iba1/microglia, CD34/endothelial cells). In a normal cervical spinal cord, we herein determined that SMI32+ MNs have a soma surface between 117.8 and 805.2 μm^2. The quantification of the cell-size distribution by histology was also performed on SCI samples, in which drastic morphological changes occurred such as in the cases of neuron loss or glial activation. In such pathological conditions, astrocytes underwent hypertrophy, reaching a cell size up to 152 μm^2, partially overlapping MN cells (Supplementary Fig. S1). Therefore, we set the lower threshold for considering cells as MNs on SXPCT images at a volume of $10 \times 10 \times 10\ \mu m^3$. Only cells localized in the inferior quadrants of the spinal cord and with a volume ranging from $10 \times 10 \times 10\ \mu m^3$ to $30 \times 30 \times 30\ \mu m^3$ were counted. It should be noted that we set up our lower cutoff value for defining MN soma a bit lower than other groups[2,5–7]; as a consequence, we probably included beta and gamma MNs. However, this methodological difference was not expected to influence the results to a considerable extent for the discussion, because the same criterion was consistently used for all MN subsets, thus ensuring the possibility of performing meaningful comparisons among different experimental groups.

Spinal cord axial images were divided into four quadrants, centered on the ependymal canal. Then, we selected two regions of interest (ROIs), in the third and fourth quadrants, corresponding to the contralateral and ipsilateral ventral horns of the spinal cord, respectively

(Supplementary Fig. S2). For each sample, MN quantification was separately performed, within the two ROIs (350 μm thick stacks, see Supplementary Figs. S2 and S3) at the epicenter, 0.5 and 1.0 mm from the lesion epicenter, one including the lesion epicenter and other two, rostral to the epicenter and spaced by 350 μm (see Supplementary Fig. S3).

We performed an automated 3D MN counting procedure on uninjured and injured (30 min and 7 days) spinal cords, exploiting a size-selective routine working on Fiji (3D Object counter).[33]

The quantification inside the epicenter and ipsilaterally to the lesion was also done by using 2D cell counting from the maximum intensity projection along the z axis. This approach was especially useful for recovering part of the signal of the MNs, which is mainly covered by inflammatory cells. Also in this case, the images were binarized and only objects whose dimensions were between $10\times10\,\mu m^2$ and $25\times25\,\mu m^2$ were considered in the counting (in this case we used the Analyze particles plugin of Fiji).

Registration between SXPCT images and histological sections stained with retrograde tracing of cholera toxin subunit beta (CTB). We developed a co-registration method between SXPCT images and serial matched-levels of histology sections in which phrenic MNs were retrogradely fluoro-labeled (see Supplementary Appendix S1). The rostro-caudal arrangement of the phrenic column was discriminated on tomographic spinal cord volume. This helped to identify the putative localization of phrenic MNs in various plans (frontal, parasagittal, transverse views) along the mid-cervical cord. Before registration, both the SXPCT and histological images were previously semi-automatically segmented using an edge classification algorithm and the area outside the spinal cord was masked out. Then, the histological sections were co-registered onto the tomographic images using the registration software FLIRT (http://fsl.fmrib.ox.ac.uk/fsl/flirt/) by a 2D linear transformation with 6 degrees of freedom (1 rotation, 2 translations, 2 scale and skew, i.e., oblique deformation; more details can be found in Supplementary Fig. S4 and in Supplementary Appendix S1). Based on the co-registered ROIs in individual slices, a 3D volume was generated to subsequently allow for counting of MNs within the phrenic column.

Results

Spinal cells at high-resolution SXPCT

SXPCT technique allowed simultaneous visualization of the gray/white matter interface, the penetrating blood vessels with their terminal branches into the gray matter and neuronal cell bodies (Fig. 1A–D). Spinal cord cell arrangement into nuclei and laminae in both ventral and dorsal horns, corresponding to the Rexed laminae, is shown in Figure 1. Thanks to the high spatial resolution (pixel size = $0.64\times0.64\,\mu m^2$) and a large FOV, it was possible to discriminate neuronal from non-neuronal populations, based on differential size, morphology, and contrast (Fig. 2). In particular, MNs were distinguished from glial cells (Fig. 2A,B; MNs appear as big cells in the image, whereas glial cells appear as small white dots), based on their size, shape, or location (e.g., if they are in white or gray matter; Fig. 2). The longitudinal view of the neuronal arrangement in the ventral horn (Fig. 2C) shows unambiguously the multi-polar morphology of MNs. In Figure 2D, a SXPCT capture of a MN matching its histological slice is shown for comparison. It demonstrates the correspondence in shape and location between MNs and satellite glial cells imaged with both techniques.

Quantification of MN loss following SCI

Quantification of MNs was performed on the segmented volume of the spinal cord axial section (reported in Fig. 3) at 0.5 and 1.0 mm rostral to the epicenter (Fig. 3 D–I) compared with the sham-operated controls (Fig. 3A–C; for further information see the Methods section). The visual analysis of SXPCT imaging revealed a loss of MNs ipsilaterally to the lesion as early as 30 min post-SCI (Fig. 3D–F). The quantification of the density of MNs (expressed as cell number per volume unit) revealed a loss of MNs ipsilaterally to the lesion (at the epicenter), both at 30 min and 7 days post-SCI (see histogram in Fig. 3J). At both 30 min and 7 days post-SCI, no changes in cell density were detected at 1.0 mm rostral to the epicenter compared with sham-operated control.

By targeting the C4 level, a severe trauma produced a loss of cervical MNs, including phrenic MNs, as previously demonstrated in animal models.[27,34,35] Hence, the number of phrenic MNs was also evaluated at spinal level C4. We localized the rostro-caudal arrangement of the phrenic column (Fig. 4A–C) using a co-registration method based on fluorescently labeled phrenic MNs (see the Methods section and Supplementary Appendix S1). Notably, we imaged the peculiar chain-like arrangement of MNs inside those phrenic columns (Fig. 4C). We further analyzed the SCI-induced cell death at 7 days post-SCI (Fig. 4D) and found that ipsilateral phrenic MNs were not detectable anymore with SXPCT imaging at 7 days post-SCI (not shown). In comparison with an uninjured spinal cord, only 2% of MNs in the ipsilateral phrenic column were spared, whereas, in the contralateral side, there was a non-significant decrease (Fig. 4D).

Quantification of lesion volume using 3D SXPCT

Next, we characterized the morphology and the extension of the lesion at different time-points. SXPCT imaging

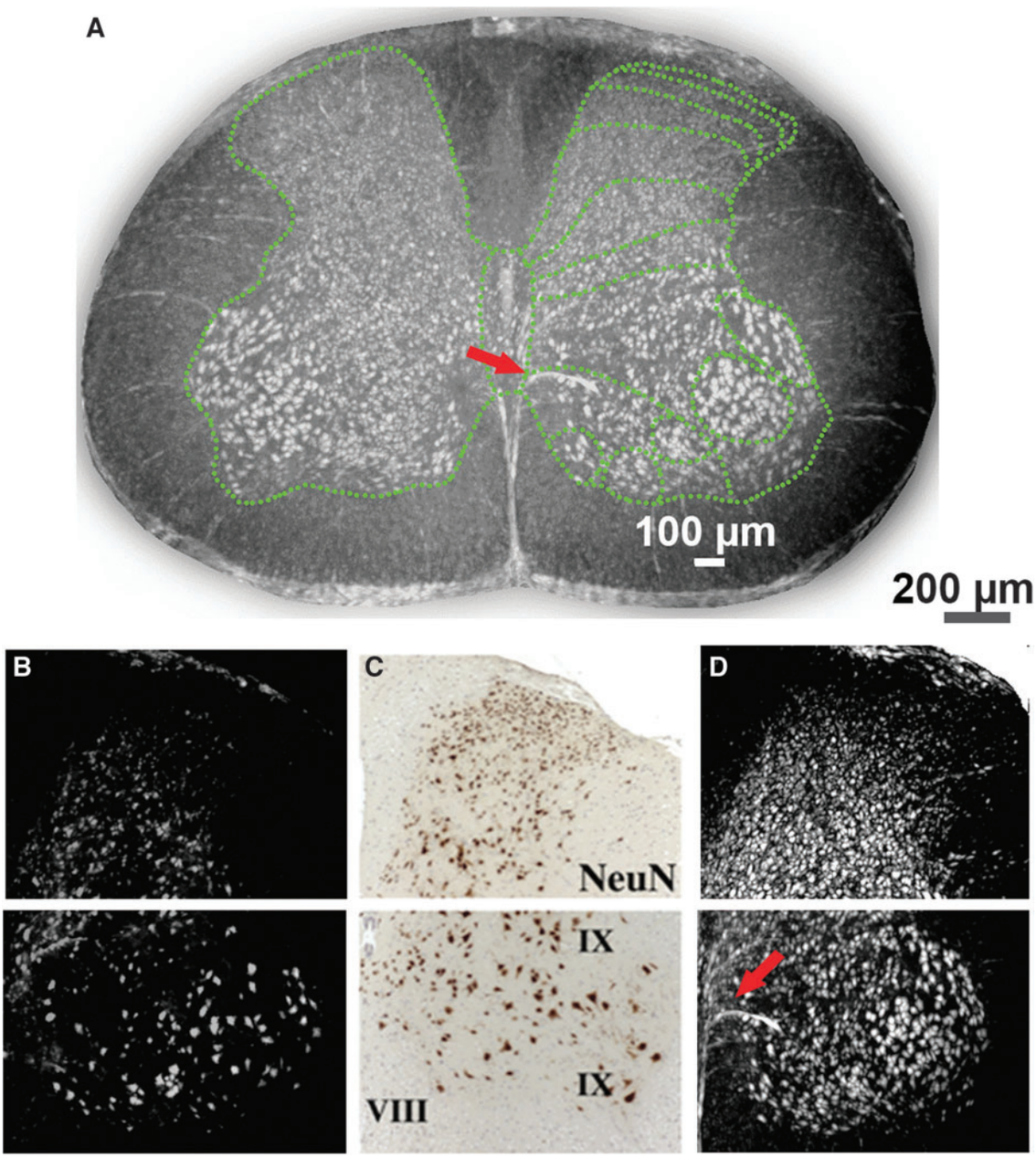

FIG. 1. Tomographic slab of normal mouse spinal cord. **(A)** 450-μm thick tomographic slab with the overlay of Rexed laminae according to the Paxinos atlas. Red arrows indicate branches from the sulcal artery. **(B, D)** Tomographic slabs 15-μm thick and 450-μm thick, respectively. The thin SXPCT slab allows to visualize well-contrasted single neurons, whereas the thick slab allowed appreciation of the neuron's architecture into laminae in both ventral and in dorsal horns (B, D). Neurons have been segmented in tomographic images and a comparison between tomography illustrations and 10-μm thick histological sliced preparations immunolabeled with NeuN are shown **(C)** as an identical pattern of those in B and D, demonstrating the validity of all the methods of investigation. SXPCT, synchrotron X-ray phase-contrast tomography.

4C ▶

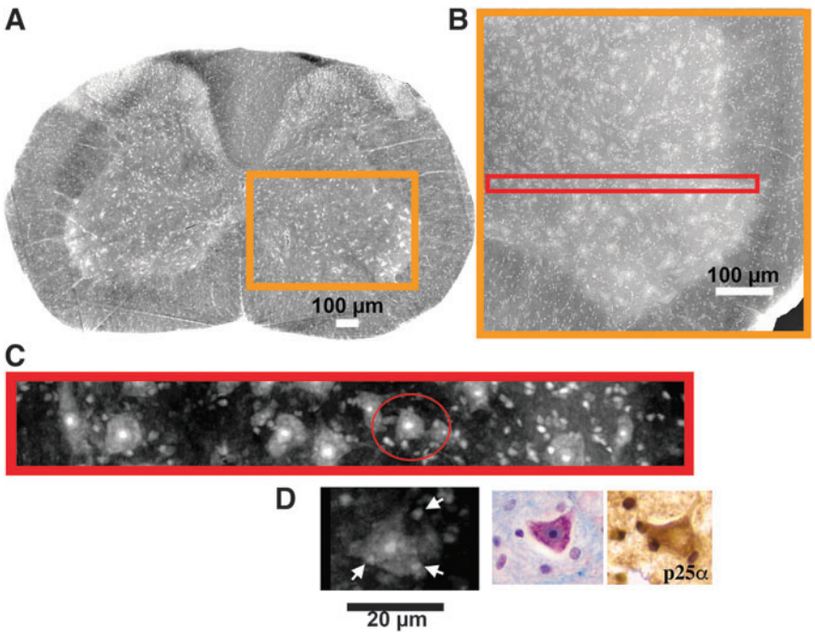

FIG. 2. Visualization of spinal cells at high-resolution by SXPCT and histology. **(A, B)** Representation of the maximum intensity of orthogonal projection to z axis. (A) 13-μm thick tomographic slab at C4 level. (B) High magnification (10×, pixel size 0.6 microns) from ventral horns (orange square in A), allowing for appreciation of the distribution of contrasted objects whose size, shape, and arrangement are compatible with neurons and satellite glial cells. **(C)** Longitudinal view of the distribution of the neuronal arrangement in the red box in B. (**D**, left panel) Zoom of MN soma in B that appear more contrasted than to the neuropil, enclosing a prominent, central rounded nucleolus. Less contrasted (white dots) round objects surrounding the MN cell bodies are compatible with the size of glial cells, and likely include satellite oligodendrocytes (white arrows in D, left panel) as demonstrated by the Nissl staining (in D, middle panel) and p25α immunohistochemistry (marker of mature oligodendrocyte) on the same sample (in D, right panel). MN, motor neuron; SXPCT, synchrotron X-ray phase-contrast tomography.

4C ▶

was also able to capture the hemorrhagic events rapidly occurring after the initial trauma. As illustrated in Figure 5, the petechial hemorrhage segmented by SXPCT is correlated with Slc4a1 immunolabeling (a marker of erythrocyte surface protein band 3), but not with Perls staining (detecting Fe3+ in hemosiderin, a by-product of hemoglobin degradation), on matching SXPCT-histological slices. Thanks to the unique features of SXPCT imaging, it was possible to observe simultaneously the hemorrhagic extravasation (i.e., containing erythrocytes; bright white in Fig. 5D,G) and the damaged tissue (black holes in Fig. 5I,J). At 30 min post-SCI (Fig. 5D–F and Supplementary Fig. S3B), large areas of hyperintense signal extending into the gray matter and irradiating along the penetrating blood vessels of the white matter were unexpectedly observed. The hyperdense signal was markedly more spread at 30 min than at 7 days post-SCI (Fig. 5 D,F,G,H–J). The Slc4a1 immunolabeling evidenced RBC extravasation—and thus reflected microhemorrhage processes (Fig. 5E,H)—that were sufficiently self-speaking and matched the SXPCT images (Fig. 5D,F).

F5 ▶ ◀ AU8

No such signal was observed in uninjured spinal cords. Knowing that acute events following contusive SCI include microhemorrhages, resulting from intraspinal blood vessel ruptures, we proved that the hyperdense signal observed in the gray matter was blood-borne material that had leaked into the spinal parenchyma.

More details can be found in Supplementary Appendix S1 and in Supplementary Figures S5 and S6. The hemorrhagic lesion was then rendered in 3D (by AMIRA software; Fig. 6), allowing the measurements of volume data. At 30 min post-injury, the cumulative total of microhemorrhagic volumes represented $0.540 \pm 0.100\,mm^3$ (Table 1). At 7 days post-injury, the total volume of the lesion was consistent across all injured mice and reached $0.45 \pm 0.01\,mm^3$ (see Table 1). The lesion at 30 min and 7 days post-SCI had the same volume but represented

◀ SF5 ◀ SF6 ◀ F6 ◀ T1

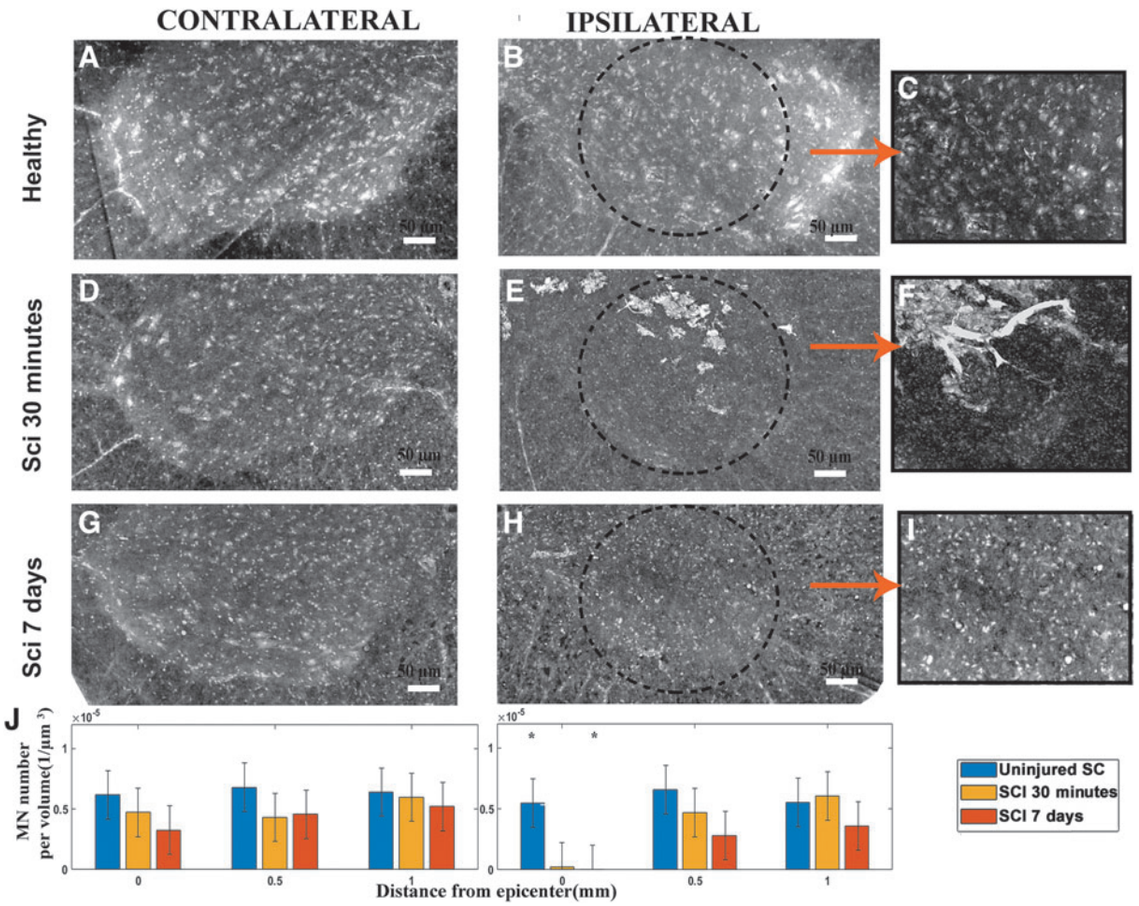

FIG. 3. Quantification of MNs. The panels **(A–H)** show the maximum intensity projections (20-μm thick) along the z direction, from uninjured (A, B) and injured spinal cords, at 30 min (D, E) and 7 days post-injury (G, H). Maximum intensity projections along the z direction are used here with the sole intention of showing MN arrangement in a single SXPCT slice whose thickness was compatible with the histological slice. However, MN quantification has been done in 3D for the uninjured sample, whereas quantification from the maximum intensity projections along the z axis has been done only in the lesion epicenter and ipsilaterally to the lesion where the high number of inflammatory cells made improper the 3D segmentation and counting. Left and right panels refer to the contralateral and ipsilateral sides of the spinal cord at the epicenter level, respectively. The 3D reconstructed tomographic volume of a typical single cell allowed us to investigate the variation of the electronic density distribution inside the neuron soma at different depths. Such variations have been analyzed at different distances from the lesion epicenter (at 0.0, 0.5, and 1.0 mm, respectively) in both the contralateral and ipsilateral side of the ventral horn, with respect to the injury. The visual analysis between the ipsilateral and contralateral sides allowed for observing that neuron loss occurs mainly inside the ipsilateral side where only few neurons survive at SCI 30 min, as one can see from comparing the enlarged black dashed area (C, F, I) of panels B, E, and H. Panel J shows the number of MNs quantified in a volume of about $880 \times 620 \times 350\ \mu m^3$ at different distances along the spinal cord contralaterally (left) and ipsilaterally (right) with respect to the lesion. Five different samples were considered for each condition, and the VOI was normalized (as the dimension of the ROI multiplied by the number of slices inside the collection stack) and reported. The final value (mean $\pm$ SEM) was then obtained by averaging across five samples. The SEM takes into account the standard deviation computed across the samples and the maximum error resulting from different thresholding values. The quantification shows a loss of cells at the epicenter as early as 30 min post-SCI and at 7 days post-SCI (*), without changes in the rostral direction to the epicenter. MN, motor neuron; ROI, region of interest; SCI, spinal cord injury; SEM, standard error of the mean; SXPCT, synchrotron X-ray phase-contrast tomography; VOI, volume of interest.

AU13 ▶

4C ▶

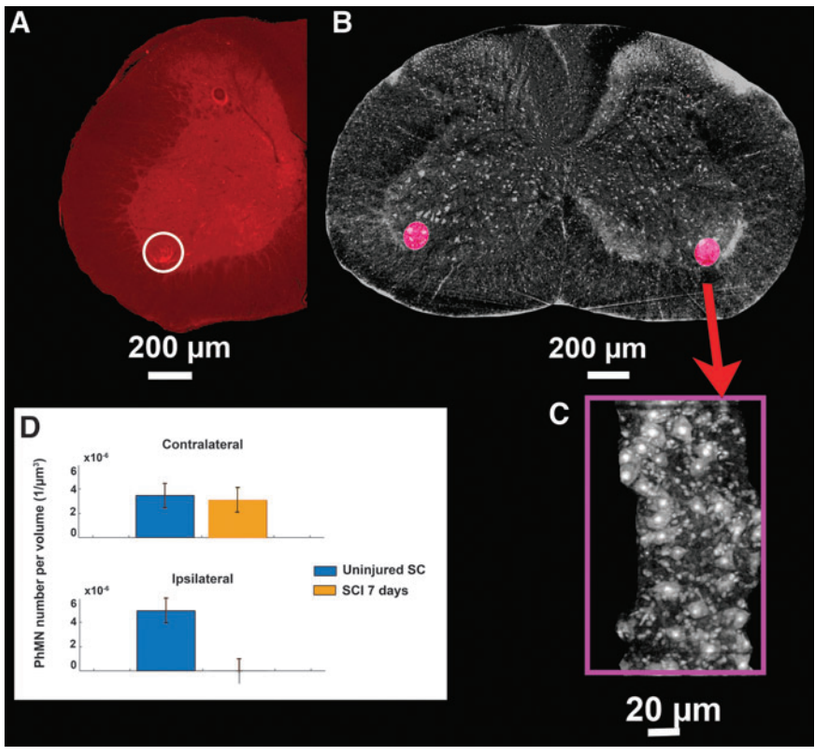

FIG. 4. Arrangement of phrenic column in the axial anatomical planes. **(A)** Histological section where phrenic neurons, surrounded by a white circle were retrogradely traced with fluorescent CTB. **(B)** Phrenic columns were identified on SXPCT tomographic slabs after co-registering serial sections on which phrenic neurons were labeled with CTB. **(C)** Three-dimensional segmentation of high-resolution (10×, $0.64 \times 0.64\ \mu m^2$ pixel size) images at the C4 level allows recognition of the chain-like aspect of phrenic MNs in the phrenic column (white inset). **(D)** The number of phrenic MNs was quantified in a volume of $136 \times 166 \times 350\ \mu m^3$. Data are expressed as mean ± SEM. Co-registration and analyses were performed on a single sample from each condition. To quantify the number of phrenic MNs, filtering procedures were applied based on MN size and the analysis was run in two VOIs, corresponding to the projected phrenic columns as done for MN counting. CTB, cholera toxin beta; MN, motor neuron; SCI, spinal cord injury; SEM, standard error of the mean; SXPCT, synchrotron X-ray phase-contrast tomography; VOI, volume of interest.

4C ▶

FIG. 5. Comparison between SXPCT and histology. SXPCT images of hemorrhage at 30 min following SCI **(D)** and 7 days post-SCI **(G, I)**, compared with the SXCPT image of an uninjured SC **(A)** and with level-matched tissue slides, immunostained with Slc4a1 **(B, E, H)** and Perls/neutral red **(C, F, J)**. The red circles in D, G, and I localize the lesion epicenter. The maximum projection of the intensity of a 30-μm thick slab (A, D, G) reveals hyperintense signals spreading into the white and gray matter (orange arrows; D, G). On level-matched spinal slices, this signal perfectly corresponds to the presence of Slc4a1+ erythrocytes that have leaked from damaged blood vessels into spinal parenchyma (H, E). The hyperintense signal seen in SXPCT does not correlate with Perl's staining at 30 min (F) or at 7 days post-SCI (J). At 7 days post-SCI, large hemosiderin deposits (red arrow) can be found in the peri-lesional reactive gliosis (J) and are detected in SXPCT as hypointense signal (red arrow; I) (30-μm thick). SCI, spinal cord injury; SEM, standard error of the mean; SXPCT, synchrotron X-ray phase-contrast tomography; VOI, volume of interest.

4C ▶

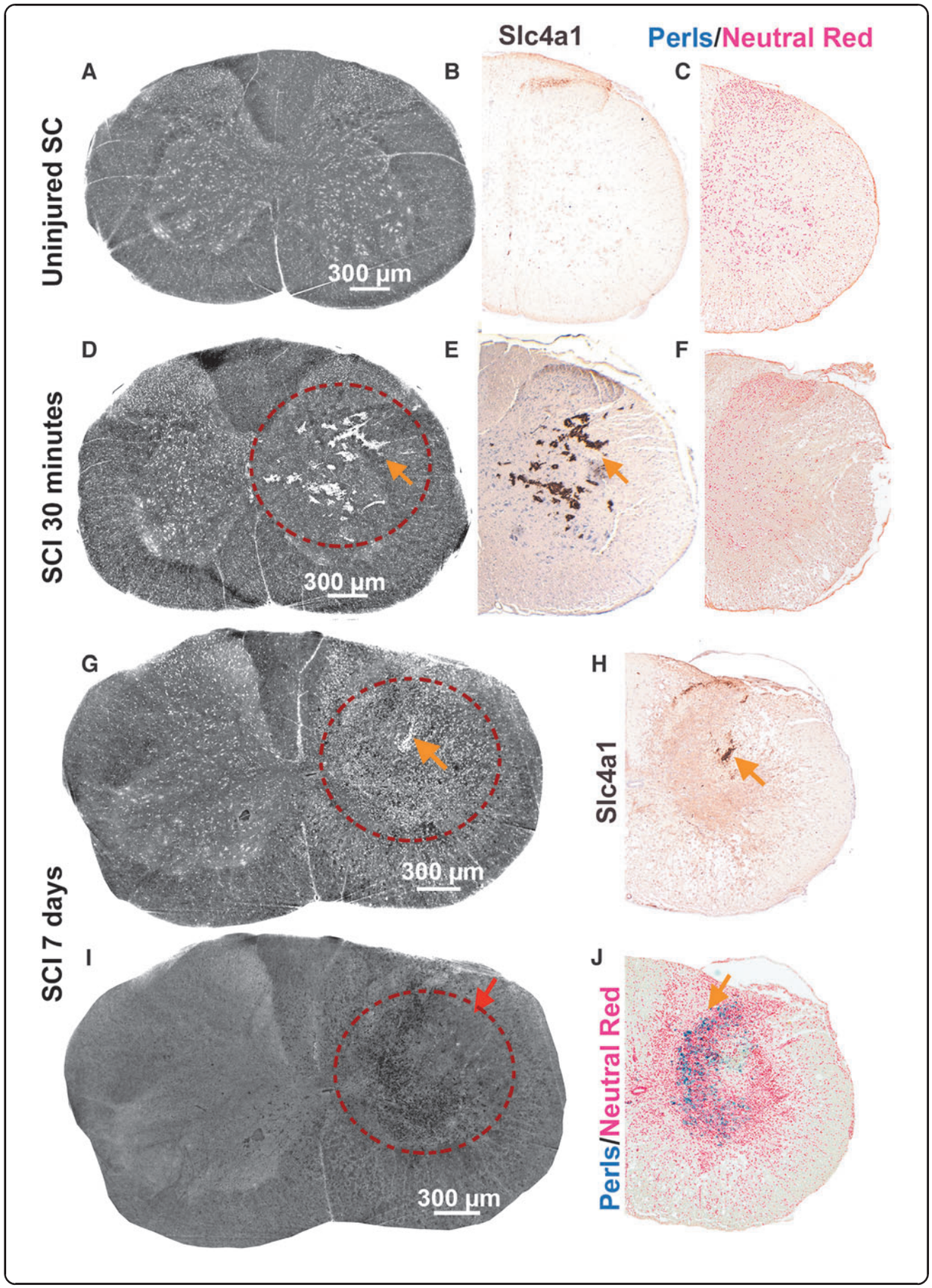
Slc4a1
Perls/Neutral Red
A
B
C
Uninjured SC
300 µm
D
E
F
SCI 30 minutes
300 µm
G
H
Slc4a1
SCI 7 days
300 µm
I
J
Perls/Neutral Red
300 µm

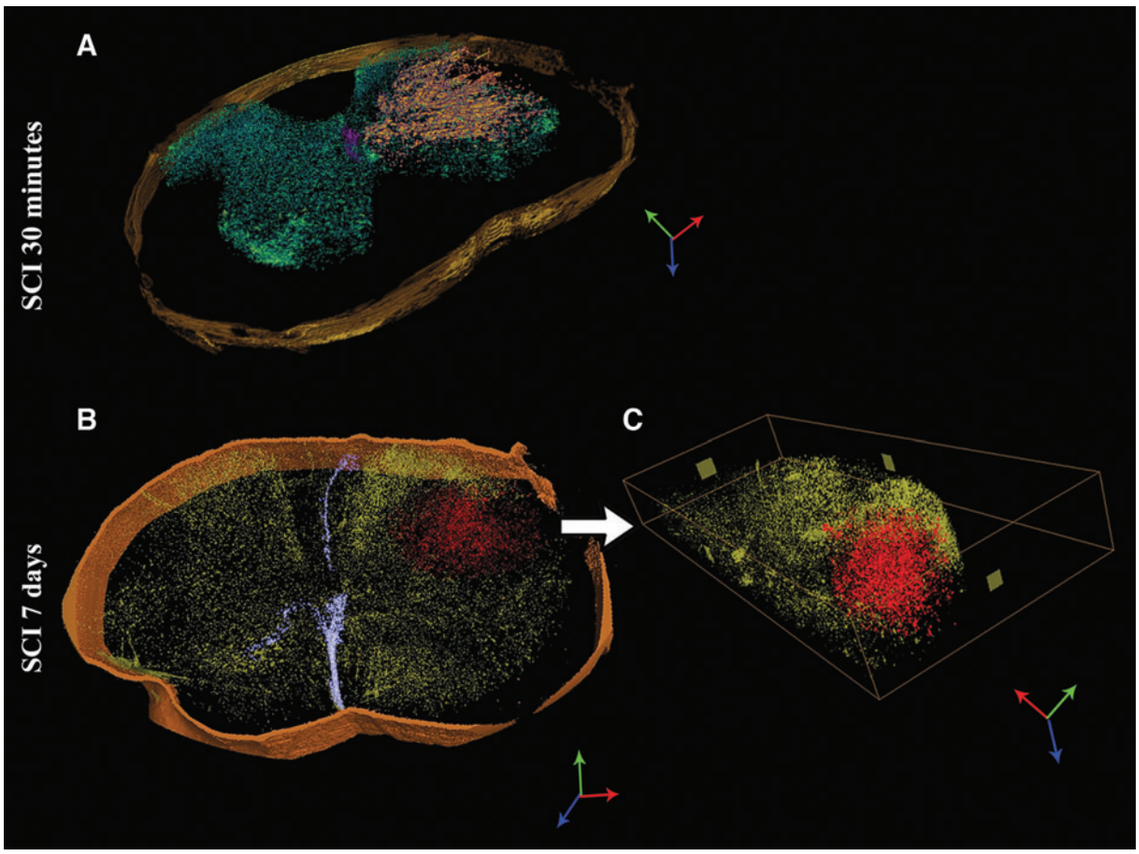

4C ▶

FIG. 6. Three-dimensional rendering reconstruction (x, y, and z axes are indicated by arrows in red, green, and blue, respectively) of the lesion at the epicenter (AMIRA software) of SCI 30 min **(A)** and SCI 7 days **(B, C)**. In magenta (A) and red (B, C) the hyperintense signal is arising from erythrocyte extravasation; inflammatory cells are in in green (A); yellow are the neuronal cells (B,C), and the central canal is in purple. SCI, spinal cord injury.

AU14 ▶

two different stages of the SCI, as a consequence of hemorrhagic events along with the secondary response of glial cells at the same 7-day delay. Considering the peri-lesional crown-shaped cellular infiltrate at 7 days post-SCI, we sought to explore how the glial scar process distributed around the lesion epicenter. We measured the thickness of the peri-lesional rim in different geometric planes using 3D SXPCT and found that, in general, the rim thickness was homogeneously formed in the axial plane (Supplementary Fig. S7G, Table 2). Intriguingly, ◀SF7 ◀T2

Table 1. Quantitative Assessment of Lesion Volume from SXPCT Tomographic Slabs and Serial Histological Sections

Sample	*SXPCT (mm^3)*	*Histology (mm^3)*
SCI 30 min	0.54 ± 0.10	/
SCI 7 days	0.45 ± 0.01	0.50 ± 0.10

Data are expressed as mean ± SD ($n = 3$ for SXPCT and $n = 4$ spinal cords for histology). The lesion volume at 7 days post-SCI was calculated by cumulating the volume of the hemorrhagic epicenter and the peri-lesional cellular infiltrate seen in SXPCT (Fig. 6B, Supplementary Video S1). For comparison and validation, the lesion volume was estimated by serial histological sections and the Cavalieri's method at 0.5 ± 0.1 mm^3 onto the same samples as described in the Methods section of Supplementary Appendix S1.

SV1 ▶

SCI, spinal cord injury; SD, standard deviation; SXPCT, synchrotron X-ray phase-contrast tomography.

Table 2. Peri-Lesional Rim Thickness along the Coronal and Axial Directions

	Rim thickness (μm) ± SD
Axial plane	
Medial	177 ± 40
Lateral	152 ± 13
Dorsal	195 ± 20
Ventral	198 ± 30
Coronal plane	
Rostral	258 ± 10
Caudal	171 ± 10

Data are expressed as mean ± SD ($n = 3$).
SD, standard deviation.

in the coronal plane, the extension of the glial scar process was greater at the rostral border of the SCI lesion (Supplementary Fig. S7H, Table 2).

Discussion

This work aimed to investigate the morphology of a SCI lesion and its temporal evolution using 3D SXPCT in combination with computational and cross-validated histology methods. From one side, SXPCT was used to assess cells or tissue damage following SCI, overcoming common problems due to the lower spatial resolution of other soft-tissue 3D imaging techniques.[36–40] On the other hand, histology combined with immunohistochemistry provides complementary information due to its specific identification of nervous cell types based on their biomarker expression profile. Major advantages of SXPCT image analysis include the direct 3D cell quantification within a volume-of-interest, avoiding many of the technical issues during sample preparation as in the case of stereology (unreliable serial sectioning, variation in staining intensities).[32,41,42]

Despite stereology being the most accurate and gold standard method for measuring cell densities in CNS organs as it uses statistical extrapolation during cell counting within fixed volumes to obtain an estimate,[43] it is subject to observer bias in which subjective differences in cell counting arise.[44] When immunolabeled cells are used, some cell types may be undercounted based on staining variability or modulation of expression along the disease course. In addition, it suffers from tissue shrinkage incurred during dehydration and from paraffin embedding that is usually not controlled, resulting in a source of error.

Therefore, estimating sample volume can pose a significant challenge in obtaining a reliable number of cells per volume unit. Even within a CNS region, cell densities can vary across the anatomical region; this is particularly the case in the distribution of neurons along the spinal columns and in the various Rexed laminae. The most accurate density map of the spinal cord would therefore not necessarily come from a design-based stereology method, but rather it would measure cell number or cell densities at all points in a 3D reference atlas. This is where our SXPCT approach can fill many gaps in the knowledge of cell distribution and cell densities in the spinal cord.

In our study, stereology was not initially the ideal approach, basically because it required serial thick-tissue sections (typically >20 μm) to be useful. For the latter, a specific experimental design, including neuron immunolabeling, needs to be tuned up to make stereology applicable. In our case, histological data came from serial 10-μm thick sections, immunolabeled for the detection of various cell populations (neurons, oligodendrocytes, astrocytes, microglia) including endothelial cells and extravasated RBCs. To validate our approach, we proposed comparison of the computer-assisted counting of NeuN+ neuron cell bodies from 10-μm histological slices with the size-based counting of cells within level-matched 10-μm slabs from SXPCT (see Supplementary Fig. S8). ◀SF8

In the present case, MNs are intermingled with other neuronal and glial populations in the ventral horn and the localization of the Rexed laminae (i.e., lamina IX) slightly varies along the rostro-caudal axis. Stereological methods thus show their limitations for MN quantification because they assume a random distribution of the objects counted within the ROI.[32] SXPCT image analysis might therefore offer a complementary or superior alternative to stereology counting, although the identification of cells relies on morphological features.[17]

Within the first 30 min post-SCI at epicenter, the quantification showed a loss of ipsilateral MNs, according to the decrease of neuroplasmic contrast. Such a neuronal loss remained at the same magnitude at 7 days post-SCI. In addition, between 7 days post-SCI and 30 min post-SCI no drop was shown in MN number within a given volume 0.5 mm away from the epicenter, which suggests no overt extension of primary lesion during the subacute phase. To specifically quantify a MN subset belonging to lamina IX, we co-registered cervical MNs with histological slices, into which phrenic MNs had been beforehand fluorescently labeled. The final result represents an estimation of the phrenic MN density at level C4. However, the number may be overestimated, taking into account the inclusion of neurons intermingled with phrenic MNs and the heterogeneous distribution of phrenic MNs along the phrenic column. Accordingly, following C4 injury, SXPCT-based image quantification estimated that about 98% of phrenic MNs were lost ipsilaterally within the considered volume. SXPCT allowed the achievement of the simultaneous visualization of different pathological processes (MNs loss and petechial hemorrhage) using a single image acquisition.

Following a spinal contusion, vascular integrity is compromised.[45] The rupture of small intramedullary capillaries, very susceptible to traumatic damage, leads to intraparenchymal blood extravasation, unlike large extramedullary vessels (i.e., anterior or posterior spinal arteries) that usually remain intact. Injured spinal cords showed areas of petechial hemorrhage more predominantly in the gray matter due to the enriched capillary network of this area. The vascular injury was not limited to the epicenter as it expanded in rostral and caudal directions resulting in an ovoidal-shaped hemorrhagic lesion. The extension of microhemorrhage was easily visualized in 3D on SXPCT tomographic slabs without the use of any contrast agent, whereas it was hardly assessed on tissue sections routinely stained. The hyperdense signal

detected on SXPCT images was likely caused by the accumulation of extravasated erythrocytes, which contain hemoglobin molecules with a dense core of iron. AU10 ► The lesion (herein deliberately referred as the hemorrhagic area), the central tissue loss, and the hypercellularized peri-lesional area did not extend in volume between the acute timing (30 min) and the subacute time-point (7 days post-SCI).

The absence of significant volumetric differences or spatial spreading between 30 min and 7 days suggests that the petechial hemorrhage could be one of the earliest predictors of lesion extension 7 days later. A similar result has been obtained in a recent work based on SXPCT imaging,[19] in which the tissue pathology following a cervical level (C6) contusion injury was studied over acute to chronic (24 h to 5 weeks) post-injury time-points. In this case, four injury time-points were considered including 24 h post-injury, 72 h post-injury, and 1 week and 5 weeks post-injury. Lesions at different time-points were compared with each other and with the sham sample. In that comparison, the authors found that tissue damage area did not change between 24 h and 1 week after injury, which is consistent with our results. Of course, we cannot rule out that the lesion together with the neuronal loss keeps extending beyond the 7-day time-point.

Lastly, we observed that the peri-lesional glial scarring was built as an inhomogeneous process, showing the highest cellular infiltration and thickness rostrally to the epicenter, compared with all other directions. Even though the glial scar border is only mature several weeks' post-injury, this finding will help to refine therapeutic strategies targeting glial scar process.[46]

However, one of the limitations of the present study is the use of the mouse as a rodent model of SCI. It is known that the pattern of spinal tissue reaction and remodeling post-SCI differs between mice and rats or humans. Rats are prone to develop large fluid-filled cystic cavities at the injury epicenter (thereby mimicking the human pathology)—in more than 90% of cervical contusion SCIs according to our previous reports—whereas mice do not.[27,34,35] The exact reason for such discrepancy between closely related rodent species is so far not known.

Advances in correlative microscopy, non-invasive imaging, and 3D image reconstruction pave the way for collecting accurate cell density information, including counting and spatial distribution, inside the spinal cord, with the aim of building a high-resolution cell atlas, similar to the initiatives that have started for the brain (e.g., EBRAINS projects). Combined with microscopy techniques that count cells labeled with multiple markers, SXPCT would allow cell-type specific registration in space, resulting in the building of a virtual cell spinal cord reference atlas. Thanks to progress in brain tissue clearing methods, neuron cell bodies and their projections can now be tracked in 3D in a whole-brain approach. In this vein, alignment to a standard reference atlas is being requested.[41] Beside the distribution of neurons, comprehensively mapping the distribution of glial cells or the vascularization down to the capillary scale would afford an unprecedented anatomical precision, leading to enhanced understanding of the neuron–glia relationship, the neurovascular unit, and their disease-induced changes.

Conclusions

Three-dimensional structural analysis of the spinal cord at cellular resolution might yield crucial information for the understanding of the pathological changes during the subacute or chronic stages of SCI. As proposed here, SXPCT-based image analysis offers the possibility to fill many gaps in the current knowledge of nervous cell distribution in the healthy or diseased spinal cord. We believe that the application of this technology will offer a powerful and physiologically relevant tool for the study of neuronal and glial morphological changes. In addition, it will help to evaluate non-invasive therapeutic strategies targeting nervous cells, scar-forming cells, or the inflammatory process following SCI.

Acknowledgments

The COST Action CA16122, Biomaterials and advanced physical techniques for regenerative cardiology and neurology (BIONECA), is acknowledged for networking support. The authors thank the staff of the TOMCAT beamline at PSI-SLS for their experimental support. ◄ AU11
The authors thank colleagues of the Consiglio Nazionale delle Ricerche (CNR) Nanotec (Rome Unit) for the fruitful discussions during the preparation of the manuscript and Luisa Le Donne for the English review of the manuscript. This research was made possible thanks to the access to the microscope facility of the Plateforme Technologique Morphologie – Imagerie (Université de Namur). The team would like also to acknowledge the significant help from two Université de Namur students: Thomas Duquesne and Lea Longueville.

Funding Information

The Italian Ministry of Health Young Researcher Grant 2013 (GR-2013-02358177) is acknowledged for financial support. Part of the research reported in this article was also supported by the FISR Project ''Tecnopolo di nanotecnologia e fotonica per la medicina di precisione'' (funded by MIUR/CNR, CUP B83B17000010001) and the TECNOMED project (funded by Regione Puglia, CUP B84I18000540002).

Author Disclosure Statement

No competing financial interests exist.

Supplementary Material

Supplementary Appendix S1
Supplementary Figure S1
Supplementary Figure S2
Supplementary Figure S3
Supplementary Figure S4
Supplementary Figure S5
Supplementary Figure S6
Supplementary Figure S7
Supplementary Figure S8
Supplementary Video S1

References

1. Oyinbo CA. Secondary injury mechanisms in traumatic spinal cord injury: a nugget of this multiply cascade. Acta Neurobiol Exp (Wars) 2011;71(2):281–299.
2. Norenberg MD, Smith J, Marcillo A. The pathology of human spinal cord injury: defining the problems. J Neurotrauma 2004;21(4):429–440. doi: 10.1089/089771504323004575
3. Choo AM, Liu J, Dvorak M, et al. Secondary pathology following contusion, dislocation, and distraction spinal cord injuries. Exp Neurol 2008;212(2):490–506; doi: https://doi.org/10.1016/j.expneurol.2008.04.038
4. Grossman S, Rosenberg L, Wrathall J. Temporal–spatial pattern of acute neuronal and glial loss after spinal cord contusion. Exp Neurol 2001;168(2):273–282; doi: 10.1006/exnr.2001.7628
5. Liu XZ, Xu XM, Hu R, et al. Neuronal and glial apoptosis after traumatic spinal cord injury. J Neurosci 1997;17(14):5395–5406; doi: 10.1523/JNEUROSCI.17-14-05395.1997
6. Lou J, Lenke L, Ludwig F, et al. Apoptosis as a mechanism of neuronal cell death following acute experimental spinal cord injury. Spinal Cord 1998;36(10):683–690; doi: https://doi.org/10.1038/sj.sc.3100632
7. Ling X, Liu D. Temporal and spatial profiles of cell loss after spinal cord injury: reduction by a metalloporphyrin. J Neurosci Res 2007;85(10):2175–2185; doi: 10.1002/jnr.21362
8. Fehlings MG, Vaccaro A, Boakye M, et al. (eds). Essentials of Spinal Cord Injury: Basic Research to Clinical Practice. Thieme Medical Publishers; 2013.
9. Wilson JR, Hashimoto RE, Dettori JR, et al. Spinal cord injury and quality of life: a systematic review of outcome measures. Evid Based Spine Care J 2011;2(1):37–44; doi: 10.1055/s-0030-1267085
10. Calabrese E, Adil SM, Cofer G, et al. Postmortem diffusion MRI of the entire human spinal cord at microscopic resolution. Neuroimage Clin 2018;18(963–971); doi: 10.1016/j.nicl.2018.03.029
11. Nijeholt GJ, Bergers E, Kamphorst W, et al. Post-mortem high-resolution MRI of the spinal cord in multiple sclerosis: a correlative study with conventional MRI, histopathology and clinical phenotype. Brain 2001;124(Pt 1):154–166.
12. Arthurs OJ, Thayyil S, Pauliah, et al. Diagnostic accuracy and limitations of post-mortem mri for neurological abnormalities in fetuses and children. Clini Radiol 2015;70(8):872–880.
13. Schmierer K, McDowell A, Petrova N, et al. Quantifying multiple sclerosis pathology in post mortem spinal cord using MRI. NeuroImage 2018;182(251–258); doi: 10.1016/j.neuroimage.2018.01.052
14. Barbone GE, Bravin A, Mittone A, et al. High-spatial-resolution three-dimensional imaging of human spinal cord and column anatomy with postmortem x-ray phase-contrast micro-CT. Radiology 2021;298(1):135–146; doi: 10.1148/radiol.2020201622
15. Bravin A, Coan P, Suortti P. X-ray phase-contrast imaging: from pre-clinical applications towards clinics. Phys Medicine Biol 2013;58(1):R1–R35; doi: https://doi.org/10.1088/0031-9155/58/1/R1
16. Bukreeva I, Mittone A, Bravin A, et al. Virtual unrolling and deciphering of Herculaneum papyri by X-ray phase-contrast tomography. Sci Rep 2016;6(1):1–7; doi: https://doi.org/10.1038/srep27227
17. Fratini M, Bukreeva I, Campi G, et al. Simultaneous submicrometric 3D imaging of the micro-vascular network and the neuronal system in a mouse spinal cord. Sci Rep 2015;5(8514); doi: https://doi.org/10.1038/srep08514
18. Massimi L, Fratini M, Bukreeva I, et al. Characterization of mouse spinal cord vascular network by means of synchrotron radiation X-ray phase contrast tomography. Physica Medica 2016;32(12):1779–1784; doi: https://doi.org/10.1016/j.ejmp.2016.09.015
19. Strotton MC, Bodey AJ, Wanelik K, et al. The spatiotemporal spread of cervical spinal cord contusion injury pathology revealed by 3D in-line phase contrast synchrotron X-ray microtomography. Exp Neurol 2021;336(113529); doi: https://doi.org/10.1016/j.expneurol.2020.113529
20. Cao F, Jiang Y, Wu Y, et al. Apolipoprotein E-mimetic COG1410 reduces acute vasogenic edema following traumatic brain injury. J Neurotrauma 2016;33(2):175–182.
21. Cao Y, Wu T-D, Wu H, et al. Synchrotron radiation micro-CT as a novel tool to evaluate the effect of agomir-210 in a rat spinal cord injury model. Brain Res 2017;1655(55–65).
22. Hu J, Ni S, Cao Y, et al. The angiogenic effect of microRNA-21 targeting TIMP3 through the regulation of MMP2 and MMP9. PLoS One 2016;11(2):e0149537.
23. Hu J-Z, Wang X-K, Cao Y, et al. Tetramethylpyrazine facilitates functional recovery after spinal cord injury by inhibiting MMP2, MMP9, and vascular endothelial cell apoptosis. Curr Neurovasc Res 2017;14(2):110–116.
24. Liao S, Ni S, Cao Y, et al. The 3D characteristics of post-traumatic syringomyelia in a rat model: a propagation-based synchrotron radiation microtomography study. J Synchrotron Radiat 2017;24(6):1218–1225; doi: doi:10.1107/S1600577517011201
25. Ni S, Cao Y, Jiang L, et al. Synchrotron radiation imaging reveals the role of estrogen in promoting angiogenesis after acute spinal cord injury in rats. Spine 2018;43(18):1241–1249.
26. Wu T, Cao Y, Ni S, et al. Morphometric analysis of rat spinal cord angioarchitecture by phase contrast radiography: from 2D to 3D visualization. Spine 2018;43(9):E504–E511.
27. Nicaise C, Putatunda R, Hala TJ, et al. Degeneration of phrenic motor neurons induces long-term diaphragm deficits following mid-cervical spinal contusion in mice. J Neurotrauma 2012;29(18):2748–2760; doi: 10.1089/neu.2012.2467
28. Sprimont L, Janssen P, De Swert K, et al. Cystine–glutamate antiporter deletion accelerates motor recovery and improves histological outcomes following spinal cord injury in mice. Sci Rep 2021;11(1):12227; doi: 10.1038/s41598-021-91698-y
29. Mittone A, Manakov I, Broche L, et al. Characterization of a sCMOS-based high-resolution imaging system. J Synchrotron Radiat 2017;24(6):1226–1236; doi: 10.1107/S160057751701222X
30. Brun F, Massimi L, Fratini M, et al. SYRMEP Tomo Project: a graphical user interface for customizing CT reconstruction workflows. Adv Struct Chemi Imaging 2017;3(1):1–9; doi: https://doi.org/10.1186/s40679-016-0036-8
31. Bukreeva I, Campi G, Fratini M, et al. Quantitative 3D investigation of neuronal network in mouse spinal cord model. Sci Rep 2017;7(41054); doi: https://doi.org/10.1038/srep41054
32. Ferrucci M, Lazzeri G, Flaibani M, et al. In search for a gold-standard procedure to count motor neurons in the spinal cord. Histol Histopathol 2018;33(1021–1046); doi: 10.14670/HH-11-983.
33. Bolte S, Cordelières FP. A guided tour into subcellular colocalization analysis in light microscopy. J Microscopy 2006;224(3):213–232; doi: https://doi.org/10.1111/j.1365-2818.2006.01706.x
34. Nicaise C, Frank DM, Hala TJ, et al. Early phrenic motor neuron loss and transient respiratory abnormalities after unilateral cervical spinal cord contusion. J Neurotrauma 2013;30(12):1092–1099; doi: 10.1089/neu.2012.2728
35. Nicaise C, Hala TJ, Frank DM, et al. Phrenic motor neuron degeneration compromises phrenic axonal circuitry and diaphragm activity in a unilateral cervical contusion model of spinal cord injury. Exp Neurology 2012;235(2):539–552; doi: 10.1016/j.expneurol.2012.03.007
36. Bilgen M, Dancause N, Al-Hafez B, et al. Manganese-enhanced MRI of rat spinal cord injury. Magn Reson Imaging 2005;23(7):829–832; doi: https://doi.org/10.1016/j.mri.2005.06.004
37. Fratini M, Abdollahzadeh A, DiNuzzo M, et al. Multiscale imaging approach for studying the central nervous system: methodology and perspective. Front Neurosci 2020;14(72–72); doi: 10.3389/fnins.2020.00072
38. Huber E, David G, Thompson AJ, et al. Dorsal and ventral horn atrophy is associated with clinical outcome after spinal cord injury. Neurology 2018;90(17):e1510–e1522; doi: 10.1212/WNL.0000000000005361
39. Martin A, De Leener B, Cohen-Adad J, et al. Clinically feasible microstructural MRI to quantify cervical spinal cord tissue injury using DTI, MT, and T2*-weighted imaging: assessment of normative data and reliability. Am J Neuroradiol 2017;38(6):1257–1265; doi: 10.3174/ajnr.A5163

40. Scholtes F, Theunissen E, Phan-Ba R, et al. Post-mortem assessment of rat spinal cord injury and white matter sparing using inversion recovery-supported proton density magnetic resonance imaging. Spinal Cord 2011;49(3):345–351; doi: https://doi.org/10.1038/sc.2010.129
41. Keller D, Erö C, Markram H. Cell densities in the mouse brain: a systematic review. Front Neuroanat 2018;12(83); doi: https://doi.org/10.3389/fnana.2018.00083
42. Ritzel RM, Hoover JE. An unbiased stereological estimate of the number of motor neurons in the cervical enlargement of the rat spinal cord. J Penn Acad Sci 2010;26–30; doi: https://www.jstor.org/stable/44149711
43. Mouton PR. Quantitative Anatomy Using Design-Based Stereology. In: Approximate Analytical Methods for Solving Ordinary Differential Equations. CRC Press; 2014.
44. West MJ. Stereological methods for estimating the total number of neurons and synapses: issues of precision and bias. Trends Neurosci 1999;22(2):51–61.
45. Tator CH, Koyanagi I. Vascular mechanisms in the pathophysiology of human spinal cord injury. J Neurosurg 1997;86(3):483–492; doi: https://doi.org/10.3171/jns.1997.86.3.0483
46. Adams KL, Gallo V. The diversity and disparity of the glial scar. Nat Neurosci 2018;21(1):9–15; doi: https://doi.org/10.1038/s41593-017-0033-9

AUTHOR QUERY FOR NEU-2021-0451-VER9-MAUGERI_1P

AU1: Where applicable, add a department or division name to the author affiliations.
AU2: Affiliation 11: What is ''c/o''? Is it ''care of'' as in a mailing address? Is this affiliation the same as affiliation 1, the Rome Unit of CNR-Institute of Nanotechnology?
AU3: ''Thanks to potentiality, the high resolution of SXPCT,'': This phrase is unclear. Do you mean ''Thanks to the potentiality of high-resolution SXPCT,''?
AU4: ''Animal Ethics Committee'': of which institution?
AU5: Should ''PCO.5.5 sCMOS detector'' be ''PCO.edge 5.5 sCMOS detector'' to match ''PCO.edge 5.5'' in the camera name above?
AU6: Supplementary figures were re-numbered as they must be called out in numeric order. Please check that they are re-numbered in the text correctly and that the legends for these figures are placed with the correct figure numbers/titles.
AU7: FLIRT software: The publisher does not allow in-text URLs. Please change this URL to a complete reference, revise the in-text URL to a regular reference in-text callout, and add the full reference, including the URL, to the reference list. Renumber all references (in-text and list) accordingly.
AU8: ''self-speaking'': do you mean ''self-explanatory''?
AU9: To what does ''For the latter'' refer? The SXPCT approach? ''serial thick-tissue sections''? Unclear.
AU10: Please check that punctuation is as meant for the sentence that begins with ''The lesion…''
AU11: Please spell out PSI-SLS.
AU12: add academic degree(s) for corresponding author and confirm/correct mailing address.
AU13: In Fig. 3 legend, ''made improper'' is unclear. Do you mean ''resulted in inaccurate''? Please revise for clarity.
AU14: In the legend for Fig. 6, check the edit and punctuation of the sentence that begins ''In magenta…'' Are edits correct as meant? If no, please revise for clarity.